ACS APPLIED MATERIALS & INTERFACES

Biological and Medical Applications of Materials and Interfaces

Direct Immobilization of Biomolecules Through Magnetic Forces on Ni Electrodes via Ni Nanoparticles: Applications in Electrochemical Biosensors

Madalina Maria Barsan, Teodor Adrian Enache, Nicoleta Preda, George E. Stan, Nicoleta Georgiana Apostol, Elena Matei, Andrei C. Kuncser, and Victor Constantin Diculescu

ACS Appl. Mater. Interfaces, **Just Accepted Manuscript** • DOI: 10.1021/acsami.9b04990 • Publication Date (Web): 13 May 2019

Just Accepted

ACS Publications

is published by the American Chemical Society. 1155 Sixteenth Street N.W., Washington, DC 20036

Direct Immobilization of Biomolecules Through Magnetic Forces on Ni Electrodes via Ni Nanoparticles: Applications in Electrochemical Biosensors.

*Madalina M. Barsan, Teodor A. Enache, Nicoleta Preda, George Stan, Nicoleta G. Apostol, Elena Matei, Andrei Kuncser, Victor C. Diculescu**

National Institute of Materials Physics, Atomistilor 405A, 077125, Magurele, Romania

KEYWORDS: magnetic force, nanoparticles, nickel, immobilization, biosensor.

ABSTRACT: The present work describes a new simple procedure for the direct immobilization of biomolecules on Ni electrodes using magnetic Ni nanoparticles (NiNP) as biomolecule carriers. Ni electrodes were fabricated by electroplating and NiNP were chemically synthesized. The chemical composition, crystallinity and granular size of Ni electrodes, NiNP and NiNP modified Ni electrodes (NiNP/Ni) were determined by X-ray diffraction (XRD), scanning electron microscopy (SEM) and X-ray photoelectron spectroscopy (XPS). The electrochemical characterization of Ni electrodes by cyclic voltammetry (CV) and electrochemical impedance spectroscopy (EIS) confirmed the existence of nickel oxides, hydroxides and oxohydroxide films at the surface of Ni. Magnetic characterization and micromagnetic simulations were performed in order to prove that

the magnetic force is responsible for the immobilization process. Further, Ni electrodes were employed as amperometric sensors for the detection of hydrogen peroxide, since it is an important performance indicator for a material to be applied in biosensing. The working principle for magnetic immobilization of the enzyme-functionalized NiNP, without the use of external magnetic sources, was demonstrated for glucose oxidase (GOx) as a model enzyme. XPS results enabled to identify the presence of GOx attached to the NiNP (GOx-NiNP) on Ni electrodes. Finally, glucose detection and quantification was evaluated with the newly developed GOx-NiNP/Ni biosensor by amperometry at different potentials, and control experiments at different electrode materials in the presence and absence of NiNP, demonstrated their importance in the biosensor architecture.

1. INTRODUCTION

Nanostructured materials have been extensively used in bioanalytical devices due to their ability to enhance the overall performance of the resulting (bio)sensor[1]. Among these, metal nanoparticles (MeNP) have dual function, acting as carrier or immobilization support for the bioreceptors and as signal transducer, where due to their high surface-to-volume ratios are able to amplify the resulting signals to be monitored[2]. Electrochemical devices based on MeNP make use of their increased electroactive surface, electron conductivity and catalytic properties, to tailor new biosensor architecture with superior sensitivity and selectivity, the amperometric-based biosensors being more suitable for mass production[3].

Both MeNP size and composition directly influence their physicochemical properties, e.g. quantum confinement in semiconductor nanocrystals, surface plasmon resonance in some MeNP and superparamagnetism in magnetic materials[3]. As a result, fluorescent quantum dots (QD) and plasmonic gold nanoparticles (AuNP) were broadly used in biosensor development, covering applications from diagnosis and therapy to cancer detection and treatment[2–4].

MeNP with magnetic properties were explored in different biosensor architectures in various fields, i.e. genosensor, (bio)sensors for protein detection and enzyme biosensors, conferring efficient pre-concentration and binding of the biorecognition elements at the electrode surface, providing at the same time an easy separation methodology[5–9]. By applying an external magnetic field beneath the sensing surface, the biomolecule-functionalized magnetic MeNP are attracted at the electrode interface[5,6], enabling in this way the construction of biodevices with higher thermal stability besides increased selectivity and specificity when compared to the solely immobilized native enzymes[7]. Also, new enzymatic devices incorporate a magnet in the body of the working electrode, to ensure a good attraction/immobilization of the magnetic MeNP at the electrode interface[5,8,9].

Magnetic MeNP used in biosensing include ferric and ferrous oxides[7,10] or nickel NP[11,12] modified/functionalized with glutaraldehyde, polymers, agarose, chitosan or metal oxides[7] in order to provide a biocompatible environment for the biomolecule immobilization. It is important to state that Ni and Ni oxide based materials were recently used for the non-enzymatic detection of glucose[13–17]. However, the principle of functioning which is based on the oxidation of glucose by the NiOOH species in NaOH solutions[13], does not allow a selective detection and requires the use of alkaline media.

In the present work, a new approach to simplify electrode architecture for magnetic immobilization of biomolecules is proposed. The procedure involves the preparation and characterization of metallic electrodes with magnetic properties, at which magnetic MeNP are directly attracted by magnetic forces. Magnetic electrodes can play a dual role: as immobilization support for biological molecules and as transducers of the biological reactions. Additionally, magnetic MeNP can act as carriers for the biomolecules toward the immobilization support. In our case, both magnetic electrodes and MeNP were obtained by simple and cost-effective preparation

methods, Ni electrodes by electroplating and NiNP by the chemical reduction of a Ni salt. The performance of these electrodes as transducers of biological events was investigated for detection of hydrogen peroxide. We report for the first time, to our knowledge, the direct immobilization without the use of an external magnetic source of an enzyme trough NiNP at Ni electrodes. The working principle was demonstrated for glucose oxidase as a model enzyme.

2. EXPERIMENTAL

2.1. Reagents and solutions

All reagents purchased from Sigma Aldrich were of analytical grade, and used without further purification. Reagents were: glucose, fructose, galactose, xylose, mannose, ascorbic acid, dopamine, uric acid, glucose oxidase (GOx) from Aspergillus niger Type X-S (117200 units/g), CH_3COOH, H_3BO_3, H_2O_2, NaCl, Na_2HPO_4, NaH_2PO_4, NaOH, N_2H_4, $NiCl_2$, $NiSO_4$ and polyvinylpyrrolidone. Millipore Milli-Q nanopure water (resistivity ≥ 18 MΩ cm) was used for the preparation of all solutions.

Britton Robinson buffer was prepared using a mixture of 0.04 M H_3BO_3, 0.04 M H_3PO_4 and 0.04 M CH_3COOH and adjusted with 0.2 M NaOH (all from Sigma Aldrich) to obtain buffer solutions with pH ranging from 2 to 13. Phosphate buffer saline solution (PBS) at pH 7.0 containing 0.1 M Na_2HPO_4 and NaH_2PO_4, and 0.05 M NaCl were used for the electrochemical evaluation of Ni electrodes, for H_2O_2 amperometric detection and for the amperometric detection of glucose at the GOx-NiNP/Ni biosensor. All experiments were carried out at room temperature (25±1ºC).

2.2. Instrumentation

Electrochemical experiments, cyclic voltammetry (CV) and electrochemical impedance spectroscopy (EIS), were performed in a conventional electrochemical cell with Ni/Au/Ti/SiO_2/Si

as working electrode (Ni, geometric area ~0.1 cm^2), a Pt wire as counter electrode and a Ag/AgCl (3 M KCl) as reference, with an Ivium potentiostat/galvanostat. The EIS measurements were done at a 10 mV perturbation, in the frequency range from 100 kHz to 0.1 Hz, 5 steps/decade, at different polarization potentials. The impedance spectra were analyzed by fitting using ZView software (Scribner Associates, USA).

X-ray diffraction (XRD) measurements were performed using a Bruker AXS D8 Advance diffractometer, in parallel beam setting, equipped with Cu target X-ray tube. The scattered intensity was scanned in the 2θ range of 20-60° with a step size of 0.04°, and a dwell time of 20 s.

X-Ray Photoelectron Spectroscopy (XPS) was performed in an AXIS Ultra DLD (Kratos Surface Analysis) setup equipped with an 180° hemispherical analyzer, using Al $K_{\alpha 1}$ (1486.74 eV) radiation produced by a monochromatized X-Ray source at operating power of 300 W (15kV × 20mA). The base pressure in the analysis chamber was at least 1.0×10^{-8} mbar. Partial charge compensation was reached by using a flood gun operating at 1.52 A filament current, 2.73 V charge balance, 2.02 V filament bias. The survey spectra were recorded using Hybrid lens mode, 160 eV pass energy, slot aperture, and high resolution core level spectra using the small spot lens mode, 20 eV pass energy 110 um aperture. The core level spectra have been deconvoluted using Voigt profiles, based on previously described method[18].

Zeiss Evo 50 XVP and Tescan Lyra 3XMU Scanning Electron Microscope (SEM) were used for the morphological characterization of Ni, NiNP and NiNP/Ni. The SEM images were acquired at different magnifications.

The specific magnetization of NiNPs was measured at different temperatures in fields of up to 20 kOe in a SQUID (superconducting quantum interference device) magnetomer working under the most sensitive option (RSO).

Incubation, temperature and agitation control were carried out with an Eppendorf ThermoMixer® C and the pH-measurements with a Hanna HI 9124N portable waterproof pH-meter.

2.3. Ni electrodes preparation

For the preparation of Ni electrodes, substrates of Au/Ti/SiO_2/Si were used, in which the film thicknesses were of 50 nm SiO_2, 10 nm Ti (deposited by RF sputtering) and 100 nm Au (deposited by vacuum evaporation). Ni films were obtained by electroplating on these substrates in a 3 electrode configuration cell (working electrode Au/Ti/SiO_2/Si substrate, counter electrode a Ni plate and a commercial saturated calomel electrode –SCE, as reference), using a Watts bath, at a potential of -1.0 V vs SCE at 60 ˚C for 1 min, resulting in a thickness of about 300 nm. The Watts bath contained 225 g L^{-1} $NiSO_4$, 30 g L^{-1} $NiCl_2$ and 30 g L^{-1} H_3BO_3.

2.4. NiNP chemical synthesis

NiNP were prepared by the chemical reduction of nickel chloride with hydrazine hydrate in the presence of polyvinylpyrrolidone (PVP). Thus, 0.1 g $NiCl_2$, 0.5 ml N_2H_4 and 0.4 ml 1.0 M NaOH were added in a glass beaker containing 0.01 % PVP in ethylene glycol. The reaction was carried out at 60 ˚C under vigorous stirring. After 1 h, the black powder product was collected through centrifugation, washed several times with ethanol and finally dried at room temperature. Finally, a suspension of 1 mg of NiNP powder were dispersed in 1 ml of ultrapure water (Milli-Q Reference system by Millipore, resistivity of 18,2 MΩ·cm) and sonicated in an ultrasonic bath for 1 h.

2.5. Biosensor preparation

NiNP/Ni were obtained by dropping an aliquot of 1mg/ml NiNP suspension on the magnetized Ni, followed by washing with distilled water and drying.

For the preparation of biosensors, first, a 5% w/v stock GOx solution was prepared in 0.1 M PBS pH 7.0 and stored in the freezer at -20 ˚C. In order to attach the enzyme to the NiNP, to get GOx-NiNP, equal volumes of enzyme solution and 1 mg mL^{-1} NiNP suspensions were mixed and incubated either at 4 ˚C during 24 h or at 20 ˚C for different time intervals (24, 48. 72 and to 96 h) at 1500 rpm. Ni electrodes were immersed in the GOx-NiNP suspension for 3 min at 300 rpm, obtaining the GOx-NiNP/Ni biosensors. Other two electrode configurations were investigated for comparison purpose, GOx/Ni (without the use of NiNP) and GOx-NiNP/Au (without the use of Ni).

3. RESULTS AND DISCUSSIONS

3.1. Characterization of Ni, NiNP and NiNP/Ni

Ni, NiNP and NiNP/Ni were first investigated using structural, magnetic and electrochemical methods. The structural methods aim to determine NiNP particle size and distribution, to prove their adherence on Ni, allowing as well the determination of both Ni and NiNP/Ni chemical composition. The magnetic behavior of the system formed by the Ni electrodes and NiNPs was estimated since it represents the driving-force of the immobilization procedure. Also, a thorough characterization of the electrodes in basic, neutral and acidic media is needed, especially in neutral media were they mean to be applied in the final configuration of GOx-NiNP/Ni biosensors. This will allow to choose the working potential range and to elucidate the chemical composition of Ni involved in the redox reactions.

3.1.1. Structural characterization

The crystalline status of Ni, NiNP and NiNP/Ni has been assessed by X-ray diffraction and results are displayed in **Fig. 1A**. For Ni and NiNP/Ni, the Ni film was deposited on Au/Ti/glass

substrate, NiNP being dispersed in water. NiNP were also deposited on a SiO_2/Si, **Fig.1A-inset**, in this case NiNP being dispersed in ethanol. The Ni electrode pattern assessed by grazing incidence X-ray diffraction (GIXRD) is dominated by maxima of Au 111, superimposed Au 200 with Ni 111, and Ni 200 and no remarkable changes can be discerned between the patterns of Ni and NiNP/Ni. The structure of the NiNP was investigated separately by performing the XRD analysis on a sample consisting of NiNP placed on SiO_2/Si wafer, in order to exclude the prominent influence of Ni electrode substrate, **Fig. 1A-inset**. In this case, the patterns are featured by broader Ni maxima, characteristic for a nanocrystalline material. The main diffraction maxima are Ni 111 and Ni 200 as previously described, followed by additional peaks corresponding to 220, 311 and 222. The Scherrer equation[19] was employed to estimate the Ni crystalline coherence length ("crystallite size") from the full-width at half maximum (FWHM) of the 111 and/or 200 diffraction lines. The lines width was corrected for instrumental broadening using a corundum standard reference (NIST SRM 1976). The average crystallite size estimated for the Ni and NiNP modified Ni electrodes was of ~66 nm, whilst for the NiNP was of ~10 nm.

SEM images of NiNP and NiNP/Ni are shown in **Fig 1B**. The prepared NiNP dispersed in ethanol deposited on SiO_2/Si, **Fig.1B1**, are quasi-monodispersed in size (30-50 nm). The magnetic interactions between them have as a result the formation of "bead strings" superstructures. SEM images recorded at NiNP/Ni, **Fig. 1B2, B3**, revealed two types of conformations: i) globular structures with sizes varying between 50 and 200 nm, attributed to the NiNP, which due to their magnetic properties showed the tendency to aggregate and form large NiNP islands and ii) a thin, planar morphology with short chains of about 500 nm long, covering almost the entire electrode surface, which is linked to the polymeric matrix involved in the NiNP synthesis. The Ni electrode showed a granular structure with granule size of 20-50 nm uniformly distributed over the electrode surface, **Fig. 1B3**.

The surfaces of Ni and NiNP/Ni were characterized by XPS. The XPS spectra recorded on energy ranges corresponding to Ni 2p are represented in **Fig. 1C1, C1'** and the binding energy (BE) values determined for nickel species are presented in **Table 1**.

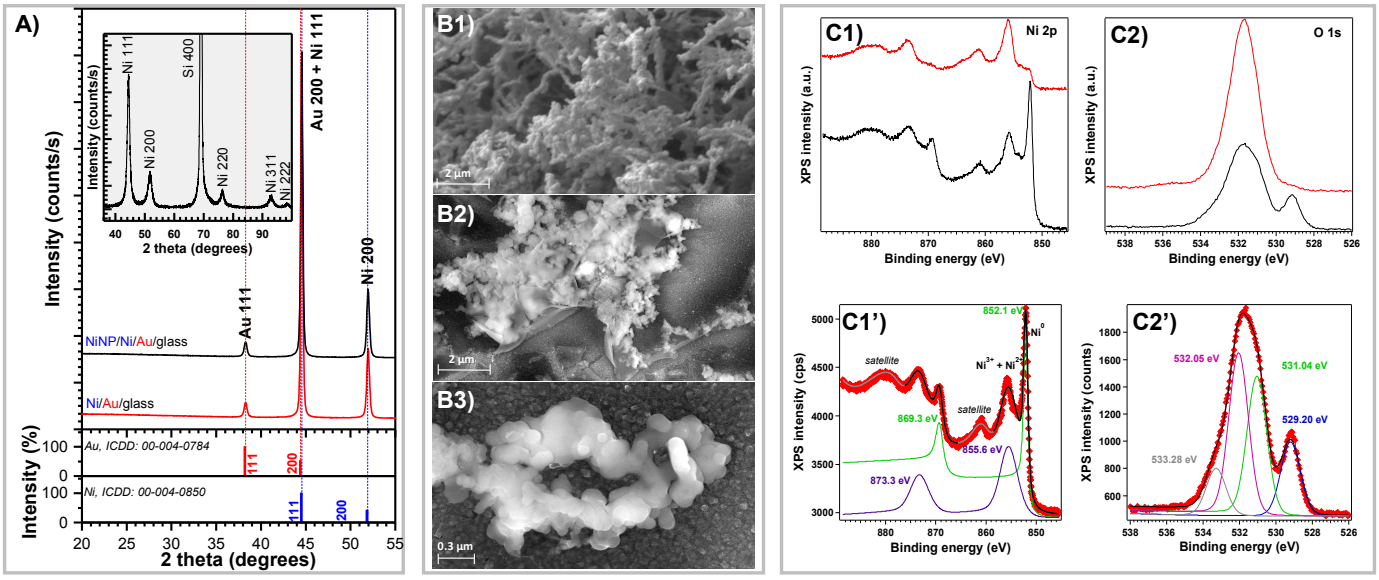

Figure 1. A) Comparative XRD patterns of Ni (—) and NiNP/Ni (—) on glass substrate; in inset is NiNP on SiO_2/Si; **B)** SEM images of **B1**-NiNP on SiO_2/Si and **B2, B3**-NiNP/Ni electrodes at different magnifications; **C)** XPS electron distribution curves (EDC) for **C1)** Ni 2pand **C2)** O 1s at Ni (—) and NiNP/Ni (—); **C1')** and **C2')** are deconvolutions of Ni 2p and O 1s for NiNP/Ni (data are analyzed with Voigt profiles and associated inelastic backgrounds.

Table 1. Binding energy (BE) values determined by XPS of nickel species found at the electrode surface.

Compound	BE Ni $2p_{3/2}$, $2p_{1/2}$ / eV	BE O 1s / eV
Ni	852.1, 869.3	
NiO		529.2
$Ni(OH)_2$	855.6, 873.3	531.0
Ni_2O_3		532.1
H_2O_{ads}		533.3

Metallic Ni is responsible for the peaks obtained at 852.1 ($2p_{3/2}$) and 869.3 eV ($2p_{1/2}$), **Fig. 1C1'**. The peaks at 855.6 ($2p_{3/2}$) and 873.3 eV ($2p_{1/2}$) are due to Ni^{2+} and Ni^{3+} species[20] indicating the

presence of $NiO/Ni(OH)_2$ and $Ni_2O_3/NiOOH$ layer on the electrode surface. The other peaks at 861.0 ($2p_{3/2}$) and 878.7 eV ($2p_{1/2}$), adjacent to the main peaks, are attributed to shake up satellite [21].

XPS spectra of Ni showed that metallic Ni is more abundant than Ni^{2+} and Ni^{3+} species, the peaks for metallic Ni at 852.1 and 869.3 eV having an intensity about twice that of the peaks observed at 855.6 ($2p_{3/2}$) and 873.3 eV ($2p_{1/2}$) for Ni^{2+} and Ni^{3+}, **Fig. 1C1**. After the deposition of NiNP on Ni electrode, the peaks for metallic Ni decrease significantly, and in this case the peaks of Ni^{2+} and Ni^{3+} overpass the peaks of metallic Ni, indicating that NiNP are rich in Ni^{2+} and Ni^{3+} species, **Fig. 1C1'**. The presence of Ni oxides on Ni and NiNP/Ni is also demonstrated by the XPS in **Fig 1C2**. The O 1s peaks were located at BE values specific to NiO, $Ni(OH)_2$ and Ni_2O_3[22,23], and their intensity increased substantially after the modification of Ni with NiNP, **Fig. 1C2'**.

3.1.2 Magnetic characterization and micromagnetic simulations

In order to use the nickel electrodes as support for the magnetic immobilization of biomolecules through NiNPs, the magnetic behavior of the system was investigated by estimating: *i*) the distribution of the magnetic field at the electrode surface, and *ii*) its effect on the NiNPs.

Before proceeding to these estimations, it is important to note that the magnetic force acting on each nanoparticle can be calculated via the gradient of the magnetic energy, $U = -\vec{m}\vec{B}$, according to the equation $\vec{F} = -gradU$, where $\vec{m}$ is the magnetic moment of the NiNP and $\vec{B}$ is the magnetic field created by the Ni film at the NiNP position. NiNP will be directed toward the electrode surface only if the component of the field gradient along the z direction is higher than that of the magnetic field along the x or y directions. In these conditions, the z component of the force which acts on each nanoparticle can be simplified to $F_z = m_z \frac{\partial Bz}{\partial z}$.

i) Distribution of the magnetic field at Ni electrodes

The distribution of the magnetic field was calculated via the OOMMF (Object Oriented Micromagnetic Framework) public domain software, developed by the Applied and Computational Mathematics Division of NIST [Donahue M J and Porter D G 1999 *OOMMF User's Guide, Version 1.0, Interagency Report NISTIR 6376* National Institute of Standards and Technology, Gaithersburg, MD]. Details on these calculations are supplied in *Supporting Information*. According to these data, the highest values of the gradient corresponds to the component along the *z* axis, **Fig. S1**. The field gradient component along the *Oz* axis ($\frac{\partial Bz}{\partial z}$), was estimated from the values of the field components of the Ni film electrode at two neighboring discretization lattice points from the electrode surface, which were -118.86 kA m^{-1} at z = 615 nm and -84.15 kA m^{-1} at z = 645 nm resulting in a $\frac{\partial Bz}{\partial z} = 1.13 \times 10^{9}$ A m^{-2}.

ii) Magnetic moment of nickel nanoparticles

The values of the magnetic moment of the NiNP along the *z* axis were obtained by collecting experimentally the magnetization of the nanoparticles *vs*. the applied magnetic fields. The magnetic hysteresis loops collected at different temperatures are presented in **Fig. 2**.

The results showed that the loops remained open also at the highest measuring temperature, with the coercive fields decreasing from 300 Oe at 10 K to 110 Oe at 300 K. This is a direct proof that the nanoparticles remains magnetic also at 300 K, as expected for NiNP with an average size of about 40 nm.

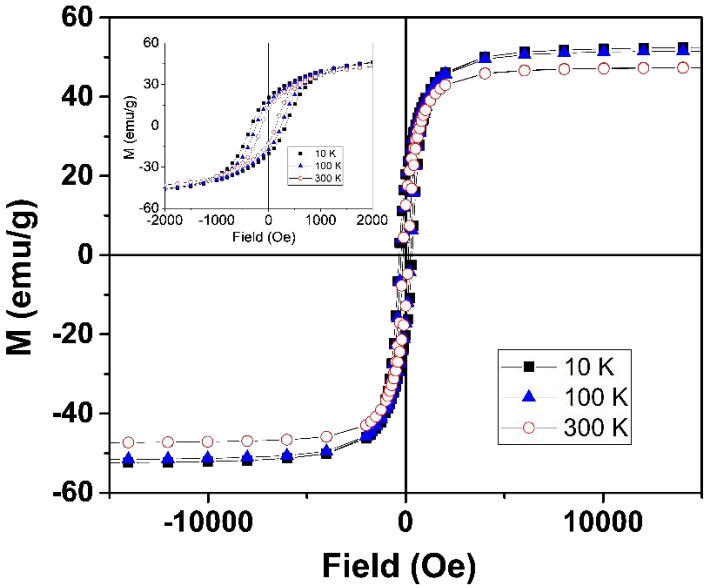

Figure 2. Magnetic hysteresis loops of NiNPs collected at 10 K, 100 K and 300 K. The inset presents the same loops over a narrower range of fields, in order to better evidence the coercive fields at all the considered temperatures.

On the other hand, the remnant magnetization is almost half from the magnetization at saturation, giving evidence that most of the nanoparticles are magnetic monodomain. The saturation field is less than 1000 Oe (0.1 T), so, in such fields all the magnetic moments of the nanoparticles are oriented along the field. The saturation magnetization is of 53 emu/g (A cm^2 g^{-1}), 10% lower than the theoretical value for Ni fcc, showing either the presence of an oxide layer and/or a disordered spin structure at the particle surface. However, with a magnetic monodomain structure and with the dominant components of the magnetic field in *Oz* direction, the dominant component of the magnetic moment along the same direction, m_z may be considered as approaching the value obtained by multiplying the specific magnetization at saturation to the mass of the nanoparticle (about 2×10^{-19} kg for a NiNP with a radius of 20 nm).

Therefore, the magnetic force $F_z = m_z \frac{\partial Bz}{\partial z}$ acting on a NiNP at 30 nm from the film surface is in the range of 10^{-11} N, almost 7 order of magnitude higher than the gravitational component, which

presents values in the range of 10^{-18} N. According to the magnetic data (presented above and in Supporting information), the magnetic force is dominant over the gravitational one up to a distance of more than a few microns from the electrode surface.

3.1.3 Electrochemical characterization

i) Cyclic voltammetry

Ni electrodes were initially tested in 0.1 M PBS pH 7.0 by CV at different scan rates, **Fig. 3A**. The potential window covered the interval between -0.50 to +1.00 V vs. Ag/AgCl. In the cathodic range, the H_2 evolution occurs for overpotentials below -0.60 V vs. Ag/AgCl as expected for metallic electrodes and the overlap in the forward and reversed scan observed for v >200 mV s^{-1} is correlated to hydrogen atoms adsorption at the Ni surface, with the subsequent reduction and desorption of the formed H_2 molecule[24,25]. In the anodic range, the oxidation of water is influenced by the scan rate, the current density increases while the overpotential of O_2 evolution decreases during consecutive scans. In between the limits of H_2 and O_2 evolution, no faradaic currents were observed at Ni electrode in neutral media.

A detailed cyclic voltammetry study was performed in 0.1 M NaOH, as shown in **Fig. 3B**. In basic media, the reversible pair of redox peaks, corresponds to the oxidation of either one of the Ni^{2+} forms, NiO or $Ni(OH)_2$, to a Ni^{3+} species such as NiOOH, as presented in the **Eq. (1)** and **(2)**:

$$NiO(s) + HO^- \rightarrow NiOOH(s) + 1e^- \quad \textbf{(1)}$$

$$Ni(OH)_2(aq) + HO^- \rightarrow NiOOH(s) + H_2O + 1e^- \quad \textbf{(2)}$$

The effect of the scan rate on Ni species redox reactions showed that the electrochemical process is driven by the diffusion of HO^- ions, as demonstrated by the linearity of current density function of square root of scan rate, **Fig 3C**.

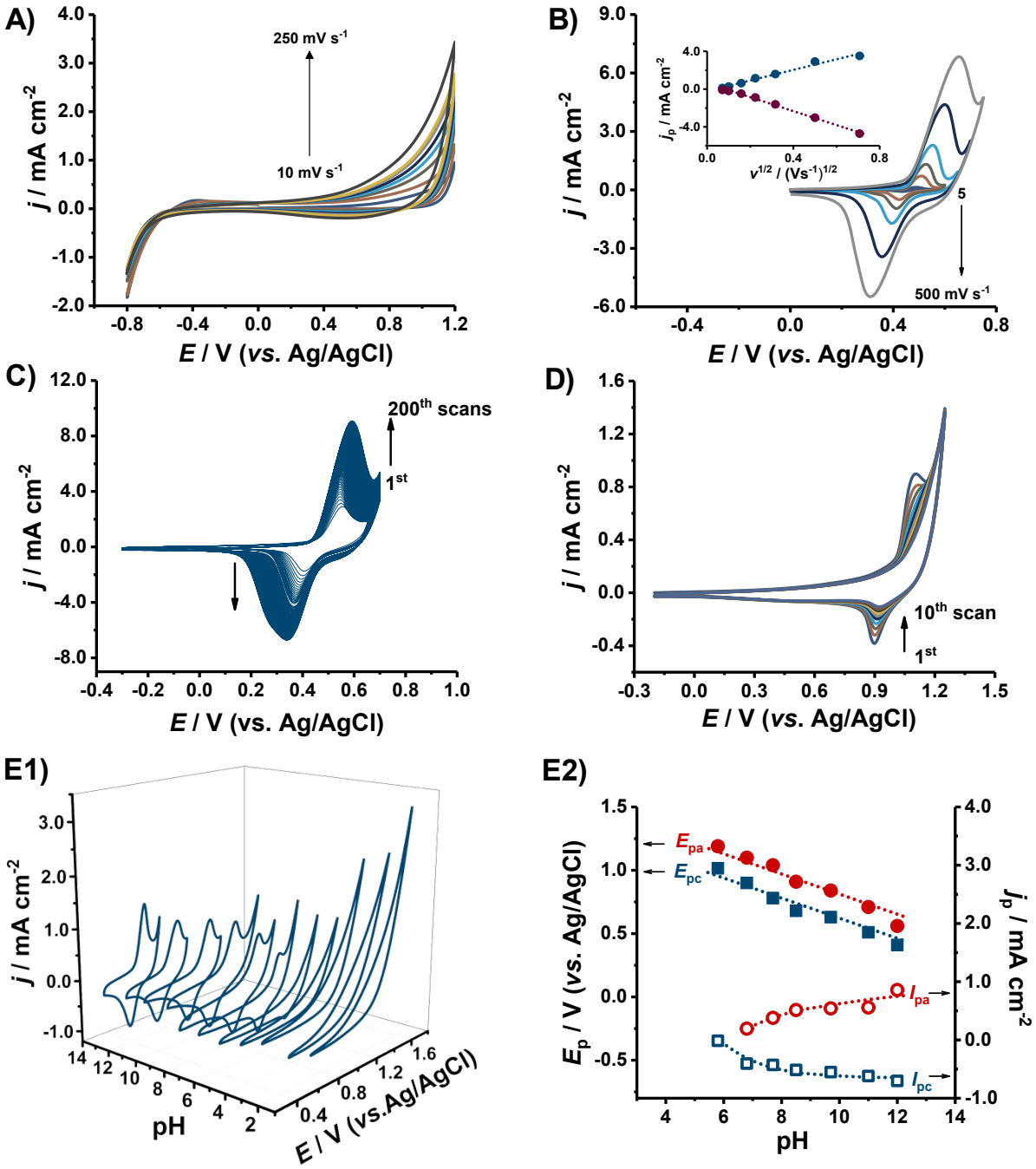

Figure 3. CV at Ni electrodes in: **A)** 0.1 M PBS pH 7.0 at different scan rates, **B)** 0.1 M NaOH at different scan rates (inset j_p vs. $v^{1/2}$), **C)** 0.1 M NaOH at 500 mV s^{-1}, **D)** 0.1 M PBS pH 7.0 at 100 mV s^{-1} after C), and **E1)** Britton-Robinson buffer with pH values from 13 to 3 at 100 mV s^{-1}, **E2)** Corresponding peak potentials and current variation with pH.

It is known that in aqueous media, NiO undergoes hydrolysis, the products $Ni_m(OH)_2^{m-n}$ depending on the solution pH[26]. In agreement, the redox processes corresponding to the $Ni^{2+/3+}$ couple, clearly seen for pH > 8.0, cannot be observed for 3.0 < pH< 7.0, **Fig. 3D, E1, E2**. This behavior can be explained considering that the solid NiOOH film formed at the electrode surface in basic media is consumed and it cannot be formed in neutral and acidic media[27].

In order to prove this effect, another experiment was performed where the potential was cycled between -0.30 to +0.70 V vs Ag/AgCl at 500 mV s^{-1} for 200 scans in 0.1 M NaOH at pH 13.0 to obtain a thick NiOOH film, as observed by the increase in the peak current intensities upon cycling, **Fig. 3C**. This peak current growth also indicates that the metallic Ni film is being consumed to generate more Ni oxide species. After the formation of NiOOH in basic media by potential cycling, the electrode was then transferred to pH 7.0 and the potential was cycled for 10 times, **Fig. 3D**. In this case, since a thicker NiOOH was formed at the surface of Ni electrode, the peaks corresponding to the $Ni^{2+/3+}$ redox process are still visible during the first scans, fading afterwards due to NiOOH consumption.

The dependence of peak current and peak potential versus solution pH was also investigated in Britton-Robinson buffer with pH values from 13.0 to 3.0, with a uniform step of 1.0, **Fig. 3E1, E2**. The CVs were recorded going from pH values of 13.0 down to 3.0, allowing the formation of NiOOH in basic media, which explains the fact that the CVs recorded at pH 7.0 and 6.0 still present low faradaic currents. For pH values below 6.0, the NiOOH film is completely consumed, as explained above, and no faradaic currents recorded. Therefore, the peak current increases with pH, the largest value being recorded at pH 13.0 while for pH < 6.0 the peak current is undetectable.

The reproducibility of the electrodes was evaluated by comparing the capacitive and faradaic currents, as well as the potential window, for 5 different electrodes, and the calculated RSD values were of 4.2, 4.8 and 5.1%, respectively.

ii) Electrochemical impedance spectroscopy.

EIS was used to investigate the physical and interfacial properties of the Ni electrodes at pH 7.0. Spectra were recorded at -0.4.0, 0.00 and +0.40 V vs. Ag/AgCl and are shown as complex plane plots in **Fig. 4A**. Taking into consideration that Ni electrodes are spontaneously covered by a NiO film which hydrolyses to $Ni_m(OH)_2^{m-n}$ as described in the CV study, the spectra were fitted using an electrical equivalent circuit, which consisted in R_Ω in series with two R_C combinations and a Warburg impedance Z_w, **Fig. 4B**. A similar circuit was used to simulate the spectra of Ni electrodes in alkaline media[28].

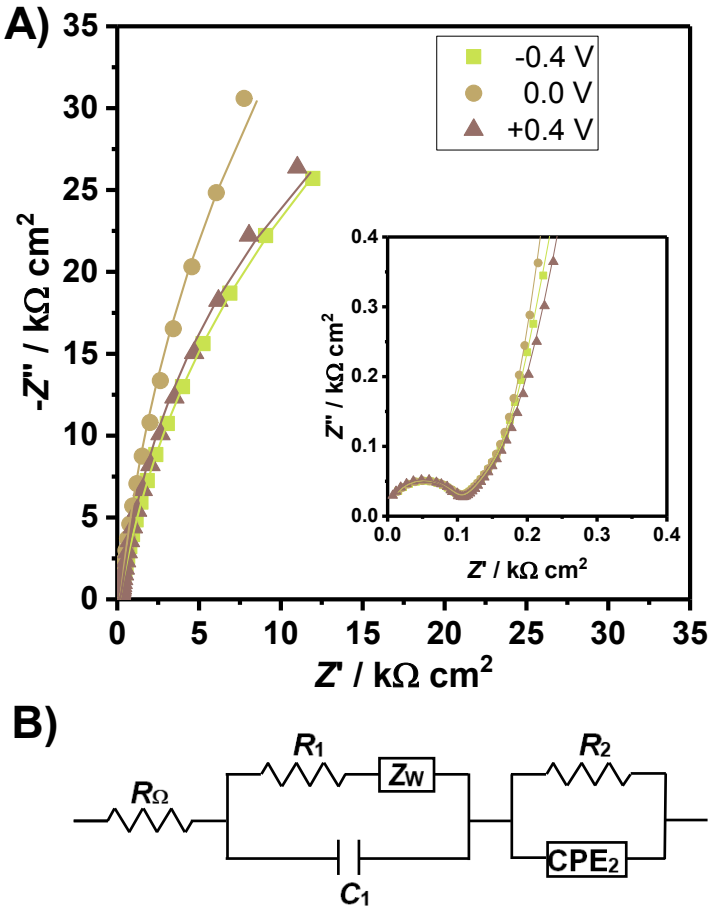

Figure 4. A) Nyquist plots recorded at Ni electrodes in 0.1 M PBS pH 7.0 in the frequency range 0.1 Hz-100 kHz at -0.40, 0.00 and +0.40 V; **B)** equivalent circuit used to fit the spectra.

R_Ω represents the ohmic drop and resistance caused by the electrical contacts and wires. The first RC combination is correlated to the Ni/Ni(OH)$_2$ interface where R_1 is attributed to the charge transfer processes between Ni and Ni(OH)$_2$ while C_1 is a pure capacitance characteristic to metal/metal oxide interface. The second RC combination corresponds to the Ni(OH)$_2$/electrolyte interface. In this case R_2 is correlated with the charge transfer process inside the Ni(OH)$_2$ film and at the Ni(OH)$_2$/electrolyte interface. CPE_2 is a constant phase element, defined in[29], corresponding to the pseudo-capacitance of the Ni(OH)$_2$ film in contact with solution. At medium frequencies the spectra show a Warburg impedance Z_w, defined as previously described[29], which can be associated to a finite diffusional processes inside the Ni(OH)$_2$ film, depending especially on the film porosity. The results obtained after fitting the experimental data are shown in **Table 2**. The value of R_Ω did not varied with the applied potential.

Table 2. Values of equivalent circuit elements obtained by fitting the spectra in Fig 3A.

E / V	R_1 / Ω cm^2	C_1 / nF cm^{-2}	Zw / Ω s$^{-0.5}$ cm^2	τ / ms	α_ω	R_2 / kΩ cm^2	CPE$_2$ / μF cm^{-2} s$^{\alpha-1}$	α_2
-0.40	8.4	247.8	23.5	8.2	0.41	5.4	276.7	0.93
0.00	8.4	243.3	25.8	9.5	0.41	11.3	197.8	0.98
+0.40	6.8	113.3	37.0	113	0.30	8.3	270.0	0.95

R_1 and C_1 have similar values for the applied potentials -0.40 and 0.00 V vs. Ag/AgCl, reflecting the fact that the interface Ni/Ni(OH)$_2$ is not affected by these two applied potentials. At +0.40 V, a small amount of Ni^{2+} is oxidized to Ni^{3+}, or an intermediate valence number, which increase slightly the current flow at this interface and subsequently decreases the R_1 and C_1. Z_w and the diffusional time constant increase with the applied potential, since the thickness of the Ni(OH)$_2$ also increased.

The R_2 associated with metal hydroxide/electrolyte interface increases, having the lowest value at -0.40 V vs. Ag/AgCl, due to dissolved oxygen reduction at this potential. At -0.40 and +0.40 V the charge separation CPE_2 at the metal hydroxide/electrolyte interface is higher than at 0.00 due to polarization phenomena.

3.2. Applications

The purpose of this study is to obtain and use magnetic electrodes with a dual role: as support for the immobilization of biomolecules via the magnetic nanoparticles and at the same time, as transducers of biochemical reactions. In this context, the performance of nickel electrodes for detection of hydrogen peroxide was investigated and the working principle for magnetic immobilization without the use of external magnetic sources was demonstrated using Ni, NiNP and glucose oxidase as a model enzyme.

GOx is an enzyme that catalysis the conversion of glucose to glucono-lactone and hydrogen peroxide in the presence of oxygen. The detection of H_2O_2 is an important performance indicator of a material to be applied in biosensing. Being the main by-product of many classical biochemical reactions catalyzed by oxidase-enzymes, the H_2O_2 detection is the basis of many biosensors functioning/monitoring.

3.2.1. Electrochemical detection of H_2O_2 at Ni electrodes

The electrochemical monitoring of H_2O_2 was performed by cyclic voltammetry, **Fig. S2**, and by fixed potential amperometry, **Fig. 5**, in 0.1 M PBS pH 7.0. Since fixed potential amperometry allowed a more sensitive response with lower detection limits, this technique was further used for sensor development.

The response to the analyte was tested over the potential range -0.50 V and +0.50 V, in order to choose the best sensing conditions, as shown in **Fig. 5A1 and B1**.

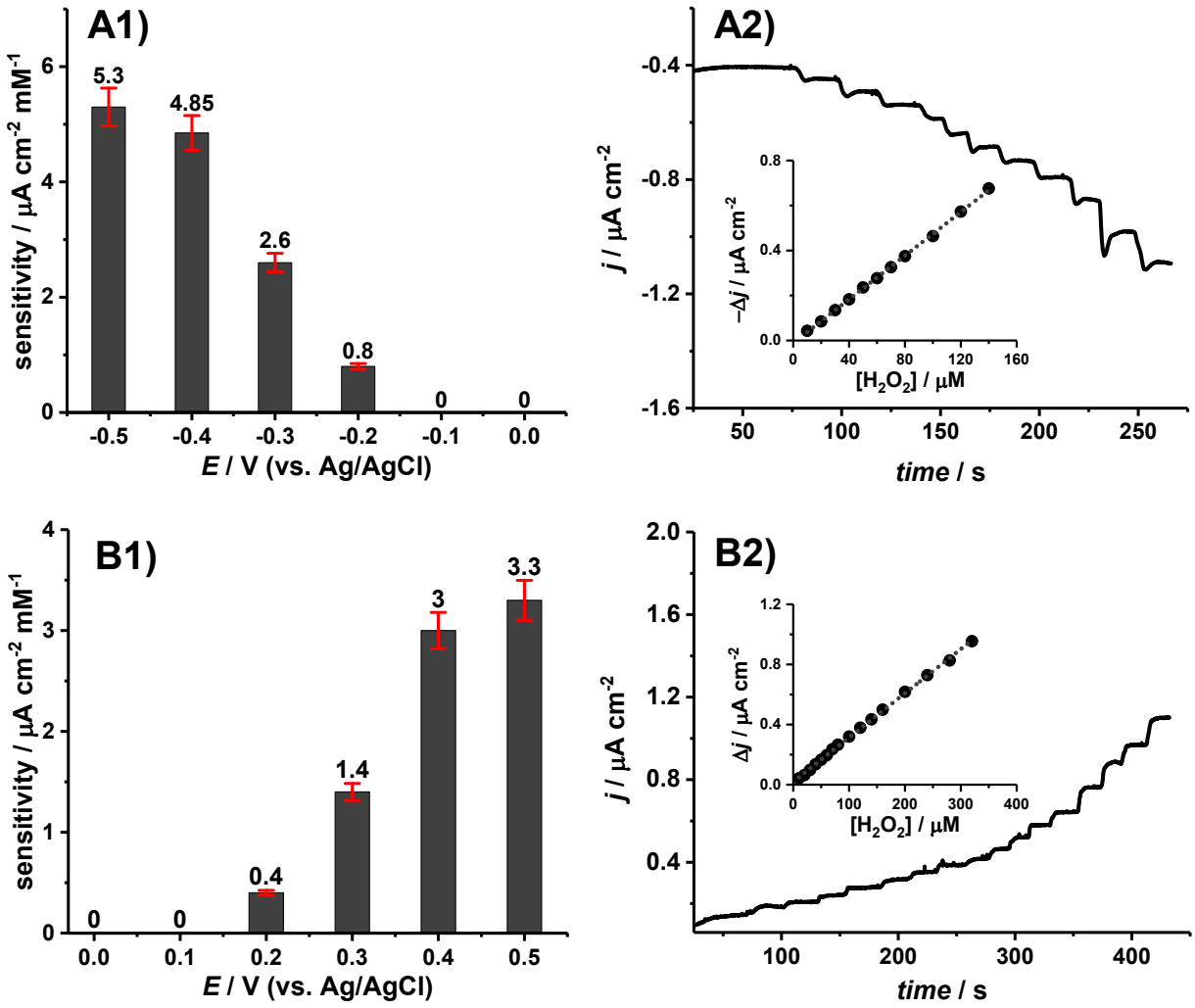

Figure 5. Potential study in 0.1 M PBS pH 7.0 at Ni electrodes - sensitivities profiles vs. applied potential in chronamerometric measurements for **A1)** negative and **B1)** positive potentials. Fixed potential chronoamperometric responses recoded at Ni electrodes upon injection of H_2O_2 at **A2)** -0.4 and **B2)** +0.4 V vs. Ag/AgCl; in insets are the corresponding calibration plots.

In the negative potential region, the cathodic change in current upon H_2O_2 injections revealed its reduction at the electrode surface, while the oxidation of H_2O_2 could be monitored at positive potentials. Highest sensitivities were observed at -0.5 and +0.5 V, but since at -0.4 and +0.4 V the

response is unneglectable smaller, and in order to reduce the applied overpotential in real sample applications, these values were chosen for further analysis.

Typical chronamperometric responses at -0.40 V and +0.40 V vs. Ag/AgCl and their corresponding calibration plots are presented in **Fig. 5A2 and B2**. The sensitivities at -0.40 and +0.40 V of Ni electrodes were 4.85 ±0.30 and 2.94 ±0.18 μA cm^{-2} mM^{-1} with limits of detection, calculated on the basis of the 3 times the standard deviation of sensitivity, of 3.2 and 9.3 μM, respectively.

Table 3. Comparison of the performance of some Ni-based H_2O_2 (bio)sensors reported in literature after 2010.

Sensor architecture	E_{app} / V	Sensitivity / μA cm^{-2} mM^{-1}	LoD / μM	pH	Ref.
NiO nanofibers/GCE	+0.60	0.04	0.33	7.4	30
AP-Ni-MOF/CPE	-0.25	n.a.	0.90	7.0	31
NiO/ITO	-0.46	41.35	5.2	9.0	32
HRP/nano-NiO/MWCNTs/PANI/GC*	-0.20	132.0	0.43	6.0	33
Cat/NiO/GCE*	-0.30	506.0	0.60	7.0	34
Mb/NiO@MWNT/GCE	-0.35	n.a.	0.39	7.0	35
Ni/Au	-0.40	4.85	3.2	7.0	this work

* enzymatic.
abbreviations: AP-adipic acid; MOF-metal organic framework; HRP-horseradish peroxidase; PANI-polyaniline; Cat-catalase; Mb-mioglobin.

The sensitivity and detection limit of the Ni electrode for H_2O_2 detection was compared with those obtained at other similar sensors, essentially constructed on nanostructured on Ni/NiO materials, **Table 3**. It can be observed that with two exceptions[33,34] which involve enzyme-based electrodes, higher sensitivity is reported for NiO/ITO[32], which operates at a more negative potential than the Ni/Au electrode presented in this work.

3.2.2. Electrochemical detection of glucose at GOx-NiNP/Ni biosensors

The biosensor construction involved two steps. In the first step, magnetic NiNP were functionalized with glucose oxidase (GOx) to get GOx-NiNP, as described in *Section 2.5*, and in the second step, GOx-NiNP/Ni biosensors were obtained by immersing the Ni electrodes during 3 min in a GOx-NiNP suspension for the direct immobilization of the enzyme through magnetic forces.

In the first step, the direct conjugation of the enzyme does not require pre-functionalization of the NP, nor the use of a linker, and occurs either via thiol chemistry when cysteine residues from the protein interact with the metal, or via histidine residues, which were found to directly bound to ions of several MeNP[40] with a high specificity to Ni^{2+} ions. Taking into consideration the XPS results, **Fig. 1C1'** in Section 3.1.1, that proved the predomination of Ni^{2+} species on NiNP surface, the second mechanism appears to be more plausible.

Table 4. Analytical parameters obtained at GOx-NiNP/Ni biosensors fabricated from GOx-NiNp suspensions incubated at different temperatures and periods of time.

incubation temperature/°C	incubation time/h	intercept/ µA cm^{-2}	sensitivity/ µA cm^{-2} mM^{-1}	RSD/ %	LD/ mM	RSD/ %
4	24	0.01±0.003	0.19±0.01	5.3	0.32±0.02	6.3
20	24	0.04±0.005	1.71±0.12	7.0	0.45±0.04	8.8
	48	0.06±0.008	3.10±0.19	6.1	0.43±0.03	7.0
	72	-0.14±0.02	6.92±0.39	5.6	0.42±0.03	7.1
	96	-0.17±0.02	7.05±0.38	5.4	0.40±0.03	7.5

With the aim of improving GOx attachment to NiNP and therefore the biosensor performance, the influence of temperature and incubation time on the direct conjugation of the enzyme with NiNP was also investigated, **Table 4**. As observed, both increase of time and temperature of incubation lead to biosensors with higher sensitivities, due to more GOx being attached on the

NiNP and therefore at Ni. Since the differences in sensitivities for 72 and 96 h of incubation at 20˚C were insignificant, the incubation for 7 h was chosen for the biosensor fabrication. The RSD values (n = 3) demonstrate the reproducibility of the biosensors obtained by employing the procedure here developed.

The presence of the enzyme at the GOx-NiNP/Ni biosensor surface was investigated and proved by XPS. The spectra in the absence and presence of GOx were recorded on energy ranges corresponding to C 1s and N 1s, **Fig. 6.** The BE values of C and N at GOx-NiNP/Ni biosensors are presented in **Table 5**.

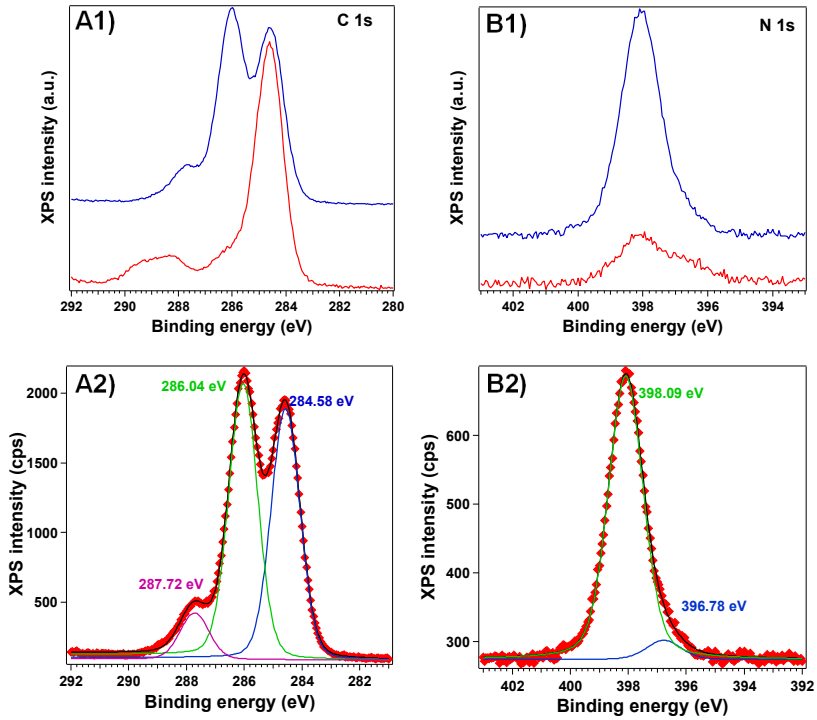

Figure 6. XPS electron distribution curves (EDCs) for **A1)** C 1s and **B1)** N 1s at NiNp/Ni (—) and GOx-NiNP/Ni (—) in the presence of GOx; **A2)** and **B2)** deconvolutions of C 1s and N 1s for GOx-NiNP/Ni (data are analyzed with Voigt profiles and associated inelastic backgrounds).

In the C 1s spectra it can be clearly seen that in the presence of the enzyme, the component peak at 286.1 eV corresponding to C-N bonds[20], predominant in the polypeptide structure, increases significantly and the peak attributed to amide groups in the polypeptide chain occurred at 287.7

eV[20]. Also, in the N 1s spectra there is a consistent increase of the band at 398.1 eV in agreement with a higher content of N atoms at the electrode surface after enzyme immobilization[20].

Table 5. Binding energy (BE) values determined by XPS for C and N at GOx-NiNP/Ni biosensor surface.

Compound	BE C 1s / eV	BE N 1s / eV
C-C	284.6	
C-O-C, C-OH, C-N	286.04	
C=O	287.72	
metal nitrides		396.78
pyridinic N		398.09

The response of GOx-NiNP/Ni biosensor was evaluated over the potential range between -0.50 and +0.50 V, **Fig. 7A**. It is important to mention that the amperometric response upon glucose injection was a cathodic change in current at negative potential values (as exemplified in **Fig 7B, C**) and an anodic signal in the positive range. Both results sustain the fact that the working principle of the biosensor is based on the detection of the H_2O_2 produced during the enzymatic reaction, as shown in **Scheme 1**.

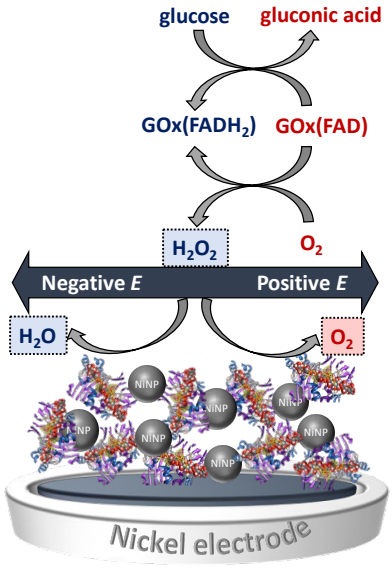

Scheme 1. Proposed enzymatic mechanism for GOx-NiNp/Ni biosensor.

Unlike the Ni electrodes in H_2O_2 sensing, that exhibited comparable analytical parameters at both negative and positive potentials, the GOx-NiNP/Ni biosensors had shown better performance at negative potentials. This can be explained by the fact that the enzymatic reaction is favored at negative potentials, since the formal potential of the enzymatic cofactor $FAD/FADH_2$ is situated at ~-0.45 V. A typical amperometric response recorded at GOx-NiNP/Ni biosensor at -0.40 V vs. Ag/AgCl in 0.1 M PBS pH 7.0 is displayed in **Fig. 7B, C**. Under optimum conditions, the biosensor had a sensitivity of 6.92 ±0.39 μA cm^{-2} mM^{-1} and a detection limit of 0.42 mM.

Following the tendency observed for the Ni electrodes in H_2O_2 sensing, a similar profile of GOx-NiNP/Ni biosensor sensitivity dependence upon the applied potential was observed, with lower responses in the positive potential region, **Figs. 5A1, B1 and Fig. 7A**. Thus, in the negative region at -0.40 V vs Ag/AgCl, the sensitivity of the biosensor was about 7.0 μA cm^{-2} mM^{-1}, with a detection limit of 0.40 mM and an apparent Michalis-Menten constant, K_M^{app} of ~6 mM. However, in the positive region at +0.40 V the sensitivity was 3.0 μA cm^{-2} mM^{-1} and the detection limit increased substantially by a factor of 5, the Michalis-Menten constant being smaller of ~3 mM. At -0.40 V vs Ag/AgCl, the relative standard deviation (RSD) obtained for three different biosensors was less than 7%, indicating the reproducibility of the biosensor construction, and an RSD lower than 5% calculated for three different measurements at the same biosensor revealed the repeatability of the analytical method based on the GOx-NiNP/Ni biosensors.

The storage stability of the GOx-NiNP/Ni biosensor was tested after storing it in air at 4 °C, and the maintained sensitivity was of 82% of the initial value after 2 weeks. The operational stability was also tested by recording 5 points calibration plots every day during one week, the sensitivity of the biosensor having 72% of the initial value.

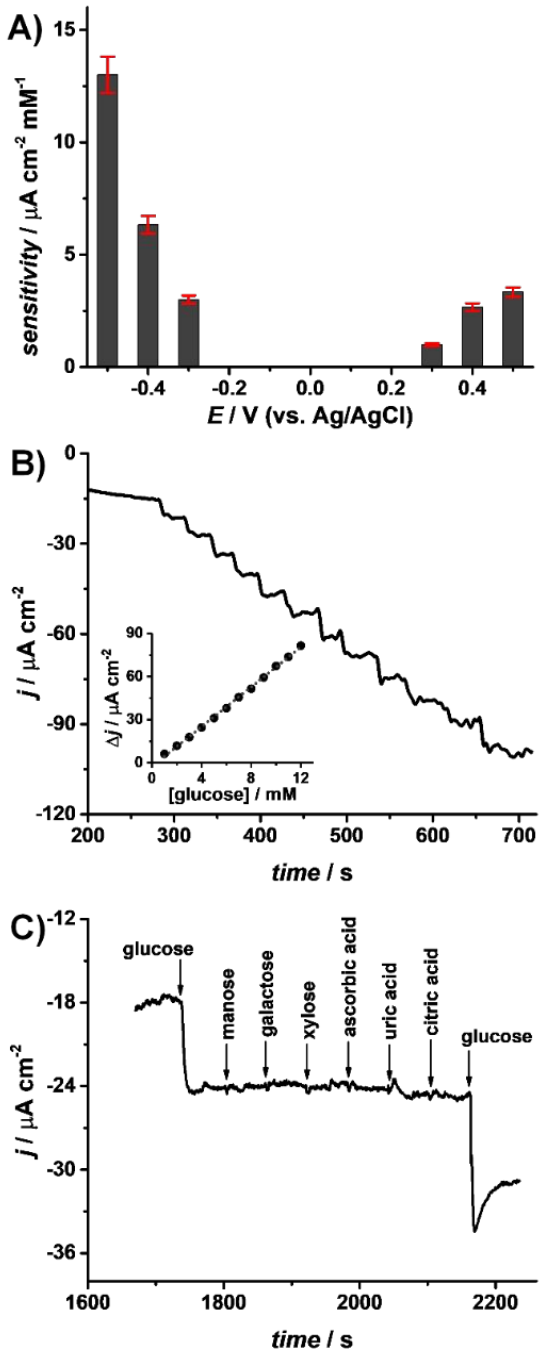

Figure 7. A) Potential study in 0.1 M PBS pH 7.0 at GOx-NiNP/Ni biosensors - sensitivities profiles vs. applied potential in chronoamperometric measurements.

B) Fixed potential chronoamperometric responses recoded at -0.40V with GOx-NiNP/Ni (GOx incubation with NiNP for 72 h at 20˚C); the inset represents the corresponding calibration plots.

C) Interference study by chronoamperometry at -0.40 V with GOx-NiNP/Ni with the injection of 1 mM glucose before and after the injection of 2 mM manose, galactose, xylose, ascorbic, uric and citric acid.

A study of possible interfering compounds, mannose, galactose, xylose, ascorbic acid, uric acid and citric acid on the biosensor response was also performed. First 1.0 mM glucose was added followed by the injection of interfering compounds, at a concentration ratio 2:1 of interfering compound: glucose, with the final injection of the same 1.0 mM concentration of glucose at the end of the experiment. The results reveled the lack of biosensor response to these possible interfering compounds at -0.40 V vs Ag/AgCl. Moreover, the biosensor response to glucose in the presence of all the interfering compounds in solution was maintained. The experiment was repeated three times with negligible interference.

For comparison, two other configurations were tested, obtained by immersing the Ni electrodes during 3 min in a solution of GOx, without the use of NiNP to get GOx/Ni biosensors, and by immersing a Au electrode during 3 min in a solution of GOx-NiNP to get GOx-NiNP/Au. Both biosensors were tested in chronoamperometric mode at different potential values and no amperometric response was recorded upon injections of glucose, indicating that the enzyme was not immobilized in the absence of NiNP or Ni. Thus, both Ni and NiNP are important for the preparation of enzyme biosensors based purely on the magnetic immobilisation of the enzyme.

Table 6. Comparison of the performance of some glucose (bio)sensors reported in literature after 2010.

Sensor architecture	E_{app} / **V**	**Sensitivity / µA cm^{-2} mM^{-1}**	**LoD / µM**	**pH**	**Ref.**
NiO/ITO*	+0.50	506.5	4.6	13.0	32
GOx/NiO/TiO_2-Gr/GCE	-0.30	4.13	1.2		36
GOx/NiHCF/CNTs	0.00	75.16	1.0	7.0	37
GOx/$Ni(OH)_2$/CGNC/Au	+0.40	16.84	2.4	13.0	38
$Ni(OH)_2$@PEDOT-rGO/GCE*	+0.55	346.00	0.60	13.0	39
GOx-NiNP/Ni/Au	-0.40 V	6.92	7.3	7.0	this work

*non-enzymatic

Abbreviations: Gr-graphene; NiHCF-nickel hexacyanoferrate; CGNC-chitosan gold nanocomposite; PEDOT-poly(3,4-ethylenedioxythiophene); rGO-reduced graphene.

The sensitivity and detection limit of GOx/NiNp/Ni biosensor for H_2O_2 detection was compared with those obtained at other similar (bio)sensors, essentially constructed on nanostructured on Ni/NiO materials, **Table 6**. It can be observed that with two exceptions[32,39] which involve non-enzymatic sensors, higher sensitivity is reported for GOx/NiHCF/CNTs[37], which involves the use of toxic hexacyanoferrates.

4. CONCLUSIONS

Magnetic Ni electrodes and NiNP were obtained by simple and cost-effective preparation methods. XRD analysis revealed a crystallite size of ≈66 nm, while SEM images of NiNP/Ni showed the existence of globular structures of 50-200 nm, with aggregation occurring due to their supramagnetic properties. XPS results indicated that metallic Ni prevailed in the Ni electrodes, while NiNP were rich in $Ni^{2+/3+}$ ions. Magnetic characterization and micromagnetic simulations were performed proving that the magnetic force is almost 7 order of magnitude higher than the gravitational component thus being the drive-force of the immobilization process.

Ni electrodes were successfully used as amperometric sensors for H_2O_2 detection over a wide potential range, with a maximum sensitivity of 4.9 μA cm^{-2} mM^{-1} at -0.4 V vs Ag/AgCl. GOx functionalized NiNP were attached to Ni electrodes only by magnetic forces leading to GOx-NiNP/Ni biosensors which operated amperometrically at both positive and negative potentials, the enzyme mechanism being based on the electrochemical detection of H_2O_2 produced in the enzymatic reaction. The absence of an amperometric signal upon substrate injection in biosensors with no NiNP or Ni electrodes, confirm the importance of both components in the biosensor architecture and prove that the immobilization of GOx through NiNP on Ni electrodes is based purely on magnetic forces.

Corresponding author: National Institute of Materials Physics Atomistilor 405A 077125, Magurele, Romania; Tel: +40-(0)21-3690185, FAX: +40-(0)21-3690177, E-mail: victor.diculescu@infim.ro

Author Contributions: The manuscript was written through contributions of all authors. All authors have given approval to the final version of the manuscript.

ACKNOWLEDGEMENTS

Financial support from the Romanian Ministry of Research and Innovation through Operational Programme Competitiveness 2014-2020, Project: NANOBIOSURF-SMIS 103528 and Core Program PN19-03 (contract no. 21 N/08.02.2019).

References

(1) Barsan, M. M.; Ghica, M. E.; Brett, C. M. A. Electrochemical Sensors and Biosensors Based on Redox Polymer/Carbon Nanotube Modified Electrodes: A Review. *Anal. Chim. Acta* **2015**, *881*, 1–23. https://doi.org/10.1016/j.aca.2015.02.059.

(2) Kim, Y. P.; Kim, H. S. Nanoparticles for Use in Enzyme Assays. *ChemBioChem* **2016**, *17* (4), 275–282. https://doi.org/10.1002/cbic.201500512.

(3) Doria, G.; Conde, J.; Veigas, B.; Giestas, L.; Almeida, C.; Assunção, M.; Rosa, J.; Baptista, P. V. Noble Metal Nanoparticles for Biosensing Applications. *Sensors* **2012**, *12* (2), 1657–1687. https://doi.org/10.3390/s120201657.

(4) Howes, P. D.; Chandrawati, R.; Stevens, M. M. Colloidal Nanoparticles as Advanced Biological Sensors. *Science (80-.).* **2014**, *346* (6205), 1247390-1-1247390–10. https://doi.org/10.1016/0250-6874(86)80002-6.

(5) Xu, Y.; Wang, E. Electrochemical Biosensors Based on Magnetic Micro/Nano Particles. *Electrochim. Acta* **2012**, *84*, 62–73. https://doi.org/10.1016/j.electacta.2012.03.147.

(6) Wang, F.; Hu, S. Electrochemical Sensors Based on Metal and Semiconductor Nanoparticles. *Microchim. Acta* **2009**, *165* (1–2), 1–22. https://doi.org/10.1007/s00604-009-0136-4.

(7) Cipolatti, E. P.; Valério, A.; Henriques, R. O.; Moritz, D. E.; Ninow, J. L.; Freire, D. M. G.; Manoel, E. A.; Fernandez-Lafuente, R.; De Oliveira, D. Nanomaterials for Biocatalyst Immobilization-State of the Art and Future Trends. *RSC Adv.* **2016**, *6* (106), 104675–104692. https://doi.org/10.1039/c6ra22047a.

(8) Kurbanoglu, S.; Mayorga-Martinez, C. C.; Medina-Sánchez, M.; Rivas, L.; Ozkan, S. A.; Merkoçi, A. Antithyroid Drug Detection Using an Enzyme Cascade Blocking in a Nanoparticle-Based Lab-on-a-Chip System. *Biosens. Bioelectron.* **2015**, *67*, 670–676. https://doi.org/10.1016/j.bios.2014.10.014.

(9) Sun, S.; Chen, L.; Shi, H.; Li, Y.; He, X. Magnetic Glass Carbon Electrode, Modified with Magnetic Ferriferrous Oxide Nanoparticles Coated with Molecularly Imprinted Polymer Films for Electrochemical Determination of Bovine Hemoglobin. *J. Electroanal. Chem.* **2014**, *734*, 18–24. https://doi.org/10.1016/j.jelechem.2014.09.034.

(10) Hasanzadeh, M.; Shadjou, N.; de la Guardia, M. Iron and Iron-Oxide Magnetic

Nanoparticles as Signal-Amplification Elements in Electrochemical Biosensing. *TrAC - Trends Anal. Chem.* **2015**, *72*, 1–9. https://doi.org/10.1016/j.trac.2015.03.016.

(11) Yang, J.; Yu, J. H.; Rudi Strickler, J.; Chang, W. J.; Gunasekaran, S. Nickel Nanoparticle-Chitosan-Reduced Graphene Oxide-Modified Screen-Printed Electrodes for Enzyme-Free Glucose Sensing in Portable Microfluidic Devices. *Biosens. Bioelectron.* **2013**, *47*, 530–538. https://doi.org/10.1016/j.bios.2013.03.051.

(12) Guo, H.; Huang, Z.; Zheng, Y.; Weng, S. Electrodeposition of Nickel Nanoparticles Modified Glassy Carbon Electrode for Nonenzymatic Glucose Biosensing. *Int. J. Electrochem. Sci.* **2015**, *10*, 10703–10712.

(13) Mu, Y.; Jia, D.; He, Y.; Miao, Y.; Wu, H.-L. Nano Nickel Oxide Modified Non-Enzymatic Glucose Sensors with Enhanced Sensitivity through an Electrochemical Process Strategy at High Potential. *Biosens. Bioelectron.* **2010**, *26*, 2948–2952. https://doi.org/10.1016/j.bios.2010.11.042.

(14) Zhu, H.; Li, L.; Zhou, W.; Shao, Z.; Chen, X. Advances in Non-Enzymatic Glucose Sensors Based on Metal Oxides. *J. Mater. Chem. B* **2016**, *4* (46), 7333–7349. https://doi.org/10.1039/C6TB02037B.

(15) Zhao, Y.; Fan, L.; Hong, B.; Ren, J.; Zhang, M.; Que, Q.; Ji, J. Nonenzymatic Detection of Glucose Using Three-Dimensional PtNi Nanoclusters Electrodeposited on the Multiwalled Carbon Nanotubes. *Sensors Actuators B Chem.* **2016**, *231*, 800–810. https://doi.org/10.1016/j.snb.2016.03.115.

(16) Xia, K.; Yang, C.; Chen, Y.; Tian, L.; Su, Y.; Wang, J.; Li, L. In Situ Fabrication of Ni(OH)2

Flakes on Ni Foam through Electrochemical Corrosion as High Sensitive and Stable Binder-Free Electrode for Glucose Sensing. *Sensors Actuators B Chem.* **2017**, *240*, 979–987. https://doi.org/10.1016/j.snb.2016.09.077.

(17) Wu, K.-L.; Cai, Y.-M.; Jiang, B.-B.; Cheong, W.-C.; Wei, X.-W.; Wang, W.; Yu, N. Cu@Ni Core?Shell Nanoparticles/Reduced Graphene Oxide Nanocomposites for Nonenzymatic Glucose Sensor. *RSC Adv.* **2017**, *7* (34), 21128–21135. https://doi.org/10.1039/C7RA00910K.

(18) Teodorescu, C. M.; Esteva, J. M.; Karnatak, R. C.; El Afif, A. An Approximation of the Voigt I Profile for the Fitting of Experimental X-Ray Absorption Data. *Nucl. Instruments Methods Phys. Res. Sect. A Accel. Spectrometers, Detect. Assoc. Equip.* **1994**, *345* (1), 141–147. https://doi.org/10.1016/0168-9002(94)90983-0.

(19) Patterson, A. L. The Scherrer Formula for I-Ray Particle Size Determination. *Phys. Rev.* **1939**, *56*, 978–982.

(20) Wang, J.; Zhao, Q.; Hou, H.; Wu, Y.; Yu, W.; Ji, X.; Shao, L. Nickel Nanoparticles Supported on Nitrogen-Doped Honeycomb-like Carbon Frameworks for Effective Methanol Oxidation. *RSC Adv.* **2017**, *7* (23), 14152–14158. https://doi.org/10.1039/C7RA00590C.

(21) Wang, L.-L.; Zhang, D.-F.; Guo, L. Phase-Segregated Pt–Ni Chain-like Nanohybrids with High Electrocatalytic Activity towards Methanol Oxidation Reaction. *Nanoscale* **2014**, *6* (9), 4635–4641. https://doi.org/10.1039/C4NR00139G.

(22) Oswald, S.; Brückner, W. XPS Depth Profile Analysis of Non-Stoichiometric NiO Films. *Surf. Interface Anal.* **2004**, *36* (1), 17–22. https://doi.org/10.1002/sia.1640.

(23) Kim, K. S.; Winograd, N. X-Ray Photoelectron Spectroscopic Studies of Nickel-Oxygen Surfaces Using Oxygen and Argon Ion-Bombardment. *Surf. Sci.* **1974**, *43* (2), 625–643. https://doi.org/10.1016/0039-6028(74)90281-7.

(24) Gao, X.; Liu, J.; Ye, S.; Song, D.; Zhang, Y. Hydrogen Adsorption of Metal Nickel and Hydrogen Storage Alloy Electrodes. *J. Alloys Compd.* **1997**, *253*, 515–519. https://doi.org/10.1016/S0925-8388(96)03034-4.

(25) Robota, H.; Vielhaber, W.; Ertl, G. Dissociative Hydrogen Adsorption on Nickel Surfaces: Absence of a Magnetocatalytic Effect. *Surf. Sci.* **1984**, *136* (1), 111–120. https://doi.org/10.1016/0039-6028(84)90658-7.

(26) Palmer, D. A.; Bénézeth, P.; Xiao, C.; Wesolowski, D. J.; Anovitz, L. M. Solubility Measurements of Crystalline NiO in Aqueous Solution as a Function of Temperature and PH. *J. Solution Chem.* **2011**, *40* (4), 680–702. https://doi.org/10.1007/s10953-011-9670-x.

(27) Wu, M.-S.; Yang, C.-H.; Wang, M.-J. Morphological and Structural Studies of Nanoporous Nickel Oxide Films Fabricated by Anodic Electrochemical Deposition Techniques. *Electrochim. Acta* **2008**, *54* (2), 155–161. https://doi.org/10.1016/j.electacta.2008.08.027.

(28) Macdonald, D. D.; Urquidi-Macdonald, M.; Bhakta, S. D.; Pound, B. G. The Electrochemical Impedance of Porous Nickel E Ectrodes in Alkaline Media. *J. Electrochem. Soc.* **1991**, *138* (5), 1–6. https://doi.org/10.1149/1.2085786.

(29) Barsan, M. M.; Carvalho, R. C.; Zhong, Y.; Sun, X.; Brett, C. M. A. Carbon Nanotube Modified Carbon Cloth Electrodes: Characterisation and Application as Biosensors. *Electrochim. Acta* **2012**, *85*, 203–209. https://doi.org/10.1016/j.electacta.2012.08.048.

(30) Vadnala, S.; Tripathy, S.; Paul, N.; Agrawal, A.; Singh, S. G. Facile Synthesis of Electrospun Nickel (II) Oxide Nanofibers and Its Application for Hydrogen Peroxide Sensing. *ChemistrySelect* **2018**, *3* (43), 12263–12268. https://doi.org/10.1002/slct.201802526.

(31) Sherino, B.; Mohamad, S.; Abdul Halim, S. N.; Abdul Manan, N. S. Electrochemical Detection of Hydrogen Peroxide on a New Microporous Ni–metal Organic Framework Material-Carbon Paste Electrode. *Sensors Actuators B Chem.* **2018**, *254*, 1148–1156. https://doi.org/10.1016/J.SNB.2017.08.002.

(32) Jana, S.; Mondal, G.; Mitra, B. C.; Bera, P.; Chakraborty, B.; Mondal, A.; Ghosh, A. Facile Synthesis of Nickel Oxide Thin Films from PVP Encapsulated Nickel Sulfide Thin Films: An Efficient Material for Electrochemical Sensing of Glucose, Hydrogen Peroxide and Photodegradation of Dye. *New J. Chem.* **2017**, *41* (24), 14985–14994. https://doi.org/10.1039/C7NJ02985C.

(33) Zhang, J.; Yang, B.; Guo, Z.; Song, Q.; Ye, X.; Zheng, S. Nickel Oxide Nanoparticles Immobilized on MWCNTs/PANI Composite Film as an Electron Transfer Facilitator for Horseradish Peroxidase: Direct Electron Transfer and H_2O_2 Determination. *J. Electrochem. Soc.* **2017**, *164* (5), B3001–B3007. https://doi.org/10.1149/2.0011705jes.

(34) Salimi, A.; Sharifi, E.; Noorbakhsh, A.; Soltanian, S. Direct Electrochemistry and Electrocatalytic Activity of Catalase Immobilized onto Electrodeposited Nano-Scale Islands of Nickel Oxide. *Biophys. Chem.* **2007**, *125* (2–3), 540–548. https://doi.org/10.1016/j.bpc.2006.11.004.

(35) Qiu, J.-D.; Cui, S.-G.; Deng, M.-Q.; Liang, R.-P. Direct Electrochemistry of Myoglobin

Immobilized in NiO/MWNTs Hybrid Nanocomposite for Electrocatalytic Detection of Hydrogen Peroxide. *J. Appl. Electrochem.* **2010**, *40* (9), 1651–1657. https://doi.org/10.1007/s10800-010-0152-4.

(36) Xu, C.-X.; Huang, K.-J.; Chen, X.-M.; Xiong, X.-Q. Direct Electrochemistry of Glucose Oxidase Immobilized on TiO2–graphene/Nickel Oxide Nanocomposite Film and Its Application. *J. Solid State Electrochem.* **2012**, *16* (12), 3747–3752. https://doi.org/10.1007/s10008-012-1813-5.

(37) Cui, X.; Liu, G.; Lin, Y. Biosensors Based on Carbon Nanotubes/Nickel Hexacyanoferrate/Glucose Oxidase Nanocomposites. *J. Biomed. Nanotechnol.* **2005**, *1* (3), 320–327. https://doi.org/10.1166/jbn.2005.038.

(38) Mathew, M.; Sandhyarani, N. A Highly Sensitive Electrochemical Glucose Sensor Structuring with Nickel Hydroxide and Enzyme Glucose Oxidase. *Electrochim. Acta* **2013**, *108*, 274–280. https://doi.org/10.1016/j.electacta.2013.07.010.

(39) Sheng, L.; Li, Z.; Meng, A.; Xu, Q. Ultrafast Responsive and Highly Sensitive Enzyme-Free Glucose Sensor Based on a Novel Ni(OH)2@PEDOT-RGO Nanocomposite. *Sensors Actuators B Chem.* **2018**, *254*, 1206–1215. https://doi.org/10.1016/j.snb.2017.08.008.

(40) Ahmad, R.; Sardar, M. Enzyme Immobilization: An Overview on Nanoparticles as Immobilization Matrix. *Biochem. Anal. Biochem.* **2015**, *4* (2), 1–8. https://doi.org/10.4172/2161-1009.1000178.

TOC

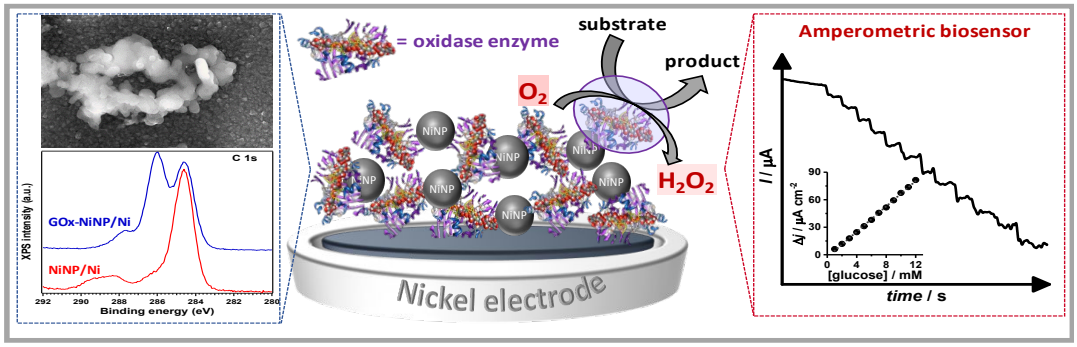
C 1s
GOx-NiNP/Ni
NiNP/Ni
XPS intensity (a.u.)
Binding energy (eV)
= oxidase enzyme
substrate
product
O_2
H_2O_2
NiNP
Nickel electrode
Amperometric biosensor
I / µA
Δj / µA cm^{-2}
[glucose] / mM
time / s